Hydrodynamics evaluation of an internal-loop airlift reactor with Newtonian and shear-thinning fluids: Experimentation vs CFD simulation

Evaluación hidrodinámica de un reactor airlift de recirculación interna con fluidos newtonianos and adelgazantes: Experimentación vs Simulación CFD

R. Guadarrama-Pérez[1], V. E. Márquez-Baños[2], J. J. Valencia-López[2], V. Sánchez-Vázquez[3], G. Martínez-de Jesús[4], J. Ramírez-Muñoz [5]*, M. Gutiérrez-Rojas[†]

[1]*Posgrado en Ciencias Naturales e Ingeniería, División de Ciencias Naturales e Ingeniería, Universidad Autónoma Metropolitana-Cuajimalpa, Av. Vasco de Quiroga, 4871, Col. Contadero, C.P. 05370, CDMX, México.*
[2]*Departamento de Procesos and Tecnología, División de Ciencias Naturales e Ingeniería, Universidad Autónoma Metropolitana-Cuajimalpa, Av. Vasco de Quiroga, 4871, Col. Contadero, C.P. 05370, CDMX, México.*
[3]*Departamento de Procesos e Hidráulica, División de Ciencias Básicas e Ingeniería, Universidad Autónoma Metropolitana-Iztapalapa, Av. San Rafael Atlixco, 186, Leyes de Reforma 1ra Sección, C.P. 09340, CDMX, México.*
[4]*Departamento de Química and Bioquímica. Tecnológico de Estudios Superiores de Ecatepec. Av. Tecnológico S/N, 55210, Ecatepec de Morelos, Estado de México, México.*
[5]*Departamento de Energía, División de Ciencias Básicas e Ingeniería, Universidad Autónoma Metropolitana-Azcapotzalco, Av. San Pablo, 180, Col. Reynosa Tamaulipas, C.P. 02200, CDMX, México.*

Abstract

The hydrodynamics of an internal-loop airlift reactor was numerically and experimentally characterized. The gas holdup, liquid velocity, shear rate, flow pattern and volumetric oxygen transfer coefficient (k_La) were evaluated as a function of the air velocity and medium rheology. Tap water and CMC solutions were used as Newtonian and non-Newtonian fluids, respectively. The standard $\kappa - \epsilon$ model was employed for modeling turbulence, and unsteady three-dimensional simulations with the Euler-Euler model were performed. Gas holdup, liquid velocity and k_La measurements were performed for validating simulations. An increase in bubble coalescence and a decrease in k_La was observed with CMC solutions. The presence of recirculation loops inside the riser for CMC solutions is reported, which was not observed with tap water. The higher the CMC concentration, the larger the recirculation region seems to be. Results show that recirculation loops play a substantial role in the reactor's hydrodynamic performance, and it turns out that the gas holdup in the riser increases with increasing the CMC concentration.

Keywords: Internal-loop airlift reactor, Shear-thinning fluids; Computational Fluid Dynamics; k_La; Flow Pattern.

Resumen

La hidrodinámica de un reactor airlift de recirculación interna fue caracterizada numérica y experimentalmente. Se evaluó la retención de gas, la velocidad del líquido, tasa de corte, el patrón de flujo y el coeficiente volumétrico de transferencia de oxígeno (k_La) en función de la velocidad de entrada de aire y la reología del medio. Se utilizó agua como fluido newtoniano y soluciones acuosas de CMC como fluidos no newtonianos. Se realizaron simulaciones tridimensionales en estado transitorio mediante los modelos Euler-Euler y $\kappa - \epsilon$ estándar para capturar el flujo multifásico y la turbulencia, respectivamente. Los resultados numéricos fueron validados con mediciones de retención de gas, velocidad del líquido y k_La. Se observó un aumento en la coalescencia de las burbujas y una disminución en los valores de k_La con las soluciones acuosas de CMC. Lazos de recirculación fueron observados en la zona de ascenso al utilizar soluciones acuosas de CMC, los cuales son mayores al incrementar la concentración de CMC. Es importante mencionar que estos lazos no están presentes al utilizar agua como medio líquido. Los resultados muestran un incremento en la retención de aire, al aumentar la concentración de CMC, debido a la formación de los lazos de recirculación.

Palabras clave: Reactor de recirculación interna, Fluido adelgazante, Dinámica de Fluidos Computacional, k_La, Patrón de flujo.

---

1   Introduction

Airlift reactors (ALRs) are pneumatically agitated vessels where the agitation is induced by a dispersed gas phase in the form of bubbles, they usually have a physical separation of upflowing and downflowing streams, promoting a better flow circulation and homogeneity inside the reactor (Doran, 2013; Kadic & Heindel, 2014). There are two main groups of ALRs, namely, external and internal loop. The external-loop airlift reactor (EL-ALR) consists of two separated columns interconnected at the top and the bottom with pipe junctions (Cerri *et al*., 2008). The internal-loop airlift reactor (IL-ALR) is a bubble column divided into two parts by a draft tube inserted along the longitudinal axis of the column, i.e., its geometry consists only of a cylindrical column with a concentric draft tube. Both EL-ALR and IL-ALR configurations consist of two fluid regions: the riser and the downcomer (Merchuk & Garcia Camacho, 2010). These fluid regions are interconnected and form a closed loop, which allows a continuous circulation of the liquid inside the reactor. The gas phase is usually injected at the bottom of the riser so that the circulation of the liquid phase is generated by the existing pressure difference between riser and downcomer (Luo & Al-Dahhan, 2008).

Due to the absence of mechanical moving parts, both EL-ALRs and IL-ALRs are considered low-shear mixing devices, and therefore, are widely used as aerobic fermenters in many shear-sensitive biochemical processes, e.g., the production of enzymes, antibiotics, proteins, biomass, and other biotechnology products (Chisti, 1989), and in other treatment processes as degradation of hydrocarbons (Lizardi-Jiménez & Gutiérrez-Rojas, 2011; Lizardi-Jiménez *et al*., 2015; Sánchez-Vázquez *et al*., 2017; Valdivia-Rivera *et al*., 2019; Medina-Moreno *et al*., 2020; Sandoval-Herazo *et al*., 2020). However, one of the main advantages of IL-ALRs with respect to EL-ALRs is their simplicity in mechanical design and geometry (Verlaan, 1987).

A detailed understanding of the hydrodynamics induced by the reactor allows for a better mass transfer rate, a good mixing, and for improving the microbial morphology and metabolism, enhancing the process yield and power consumption efficiency. It has been reported that in microbial processes, the rheological properties and physiological responses of the microorganisms change throughout the culture time (Lim *et al*., 2002). Airlift bioreactor shows high mass transfer rates with lower power consumption than agitated tanks, then, a good knowledge on the hydrodynamics and transport phenomena under different rheological medium properties is important to define the optimal configuration and operational conditions (Esperança *et al*., 2022). In this context, mathematical modelling plays a key tool in the design of new reactor configurations for a subsequently improvement of reactor design and scale up. In this study, the hydrodynamics of an IL-ALR is numerically and experimentally addressed.

Global and local gas holdup and liquid-circulation velocities (in the riser and downcomer), as well as the flow pattern and volumetric mass transfer coefficients, are considered key hydrodynamic parameters for IL-ALRs performance (Huang *et al*., 2010; Šimčík *et al*., 2011; Chen *et al*., 2016). For instance, it has been reported that the liquid circulation velocity and the flow pattern influence the mixing and mass transfer rates. On the other hand, the gas holdup is closely related to the gas phase residence time (Lu *et al*., 1995). Some relevant previous studies on IL-ALRs in the context of this work are discussed below.

Hwang and Cheng (1997) experimentally studied the hydrodynamics of an IL-ALR by using Newtonian (water) and non-Newtonian (aqueous CMC solutions, 0.1-0.8%wt) fluids. They evaluated the effect of CMC concentration on liquid velocity and gas holdup by using tracer response and manometric techniques. They reported that the liquid velocity and the gas holdup generally decrease with an increase in CMC concentration. These results are in agreement with those reported by other authors for EL-ALRs (Popović & Robinson, 1988; Gavrilescu & Tudose, 1997).

Deng *et al*. (2010) characterized the bubble behavior in an IL-ALR as a function of superficial gas velocity (2-12 cm·s^{-1}) and aqueous solution CMC concentrations (0-0.45%wt). Based on the different conductivities of the gas-liquid phase, bubble sizes and their distributions were measured with a dual-tip electrical conductivity probe. These authors reported that increasing both the superficial gas velocity and CMC concentrations led to an increase in bubble diameter and a wider bubble size distribution.

Luo and Al-Dahhan (2008) analyzed the flow structure inside an IL-ALR as a function of superficial gas velocity (0.076-5.0 cm·s^{-1}) by using computer-automated radioactive particle tracking. Water and air were used as liquid and gas phases, respectively. They found that although the flow pattern in the riser and in the downcomer is close to plug flow, i.e., the

velocity vector magnitudes are the same elsewhere, there exist stagnation zones at the reactor bottom. Wu and Merchuk (2003) studied the effect of two draft tube diameters (12 and 16 cm) on the induced flow structure in the downcomer region of a 22 cm-diameter IL-ALR by using an optical trajectory tracking system. Their experimental system was filled with water and a superficial gas (air) velocity range of 1-2.5 cm·s^{-1} was used. Their results indicated that there is no effect of the draft tube diameter on flow pattern, and this is close to plug flow under low superficial gas velocities (<2.5 cm·s^{-1}).

van Baten *et al*. (2003) performed a 2-D and 3-D CFD study in an IL-ALR operating with a water-air system in the turbulence regime in a range of superficial gas velocity of 1.0-12.0 cm·s^{-1}. They used the standard $\kappa - \epsilon$ model to simulate the turbulence and the Euler-Euler scheme for modeling the gas-liquid system, while the momentum exchange (drag) between phases was calculated from the correlation proposed by Clift *et al*. (1978) by using an average bubble diameter of 5.0 mm. Their simulation results were validated with experimental measurements of liquid velocity and gas holdup. They reported that, within their evaluated range of superficial gas velocity, there is a good agreement of 2-D and 3-D results with gas holdup and liquid velocity in riser and downcomer.

Šimčík *et al*. (2011) carried out an experimental and 3-D CFD study of the hydrodynamics of a two-phase (water-air) IL-ALR. They evaluated three turbulence models (RNG $\kappa - \epsilon$, realizable $\kappa - \epsilon$, and standard κ-ω) and two correlations for the drag coefficients (Tomiyama and Schiller-Naumann) by using an average bubble diameter of 5.0 mm. For modeling the water-air multiphase flow, the mixture model and the Euler-Euler model were used. Their numerical results were validated by using their experimental measurements of liquid velocity and gas holdup. They reported the liquid velocity both in riser and downcomer, as well as the gas holdup, as a function of the gas superficial velocity within the range 1.0-7.5 cm·s^{-1}. Their obtained results with the Mixture and Euler-Euler models are in good mutual agreement.

Šimčík *et al*. (2011) reported that the largest difference between the standard $\kappa - \epsilon$ model and the other evaluated models was around 1.4% for the liquid velocity, and 4.9% for the gas holdup, and both were evaluated in the riser. Therefore, the choice of the evaluated turbulence models had only a minor influence on the numerical results. With regards to the two evaluated correlations for the drag coefficient,

they reported that they do not exhibit a significant effect on the liquid velocity. However, their obtained holdup values in the riser were higher when the Schiller-Naumann correlation was used, with a relative difference of 13.5±2.3%, which decreased as the gas flow rate increased.

Other relevant studies where a CFD approach has been used to evaluate the hydrodynamics of internal-loop airlift reactors with Newtonian fluids are those carried out by Mohajerani *et al*. (2012) and Nalband and Jalilnejad (2019). However, although non-Newtonian rheology can have a significant effect on the hydrodynamic performance of airlift reactors, to the best of our knowledge, the number of previous numerical studies dealing with these systems with non-Newtonian shear-thinning fluids has been scarcely addressed (Xu *et al*., 2015; Han *et al*., 2017).

In the present work, this issue is brought up. The liquid recirculation velocity, gas holdup, and flow patterns of an internal-loop airlift reactor were analyzed in detail by using Newtonian and non-Newtonian (shear-thinning) fluids. Experiments and numerical simulations were carried out to evaluate the effect of both, the rheology of the medium, and the air superficial velocity on global and local hydrodynamics parameters, i.e., liquid circulation velocity, gas holdup, flow patterns and the volumetric oxygen transfer coefficient.

2 Methodology

2.1 Experimental

2.1.1 Setup experimental

The experimental arrangement employed is shown in Fig. 1. The IL-ALR was housed in a glass tube with an internal diameter of 7.2 cm. It consisted of two main parts: an *L*-shaped gas diffuser, and a draft tube. The *L*-shaped diffuser gas outlet consisted of five collinear 0.1 cm internal diameter holes and was located 12 cm above the reactor bottom. The draft tube dimensions were: 4.2, 4.5, and 20 cm for inner diameter, outer diameter, and height, respectively. The liquid height was set at 26.0 cm, for a total liquid volume of 1 L. Tap water and two aqueous solutions of carboxymethyl cellulose (CMC) at 0.25 and 0.50%wt/v, were used as working fluids, while air from a mechanical compressor was used as the gas phase; the temperature was kept constant at 23ºC.
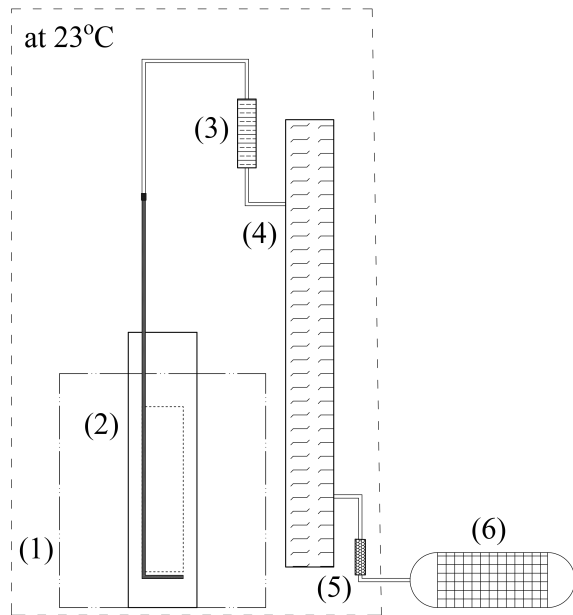
Fig. 1. Experimental arrangement. (1) square aquarium of water, (2) IL-ALR, (3) air-flow control, (4) pressure damper column, (5) wet filter, and (6) air compressor.

Table 1. Liquid phase properties.

CMC concentration [%wt/v]	Density [kg m^{-3}]	k [Pa·s^n]	n [-]
0 (water)	997.0	0.001	1.0
0.25	1001.5	0.2477	0.7488
0.50	1004.0	1.1532	0.4981

The apparent viscosity (μ_L) of the CMC solutions was measured employing an Anton-Paar MCR 502 rheometer by using a concentric cylinder geometry. The data obtained was then fitted within the shear rate ($\dot{\gamma}$) range $0.01 \leq \dot{\gamma} \leq 1000$ to a power-law model (Gavrilescu & Tudose, 1997):

$$\mu_L(\dot{\gamma}) = k(\dot{\gamma})^{n-1} \qquad (1)$$

where k and n are the consistency index and the flow index, respectively. The values obtained for k, n, and the working fluid density (i.e., liquid phase) are shown in Table 1. The correlation coefficients (R^2) of the above model with the two testing fluids in the range of validity were 0.9974 (CMC at 0.25 %wt/v) and 0.9992 (CMC at 0.25 and 0.50%wt/v).

2.1.2 Gas holdup and liquid velocity measurements

Both the gas holdup (α_G) and liquid phase velocity (U_L) were evaluated at five air superficial velocities: U_S = 0.20, 0.31, 0.41, 0.51 and 0.61 cm·s^{-1}. α_G was calculated from the difference between aerated and non-aerated operating conditions, as shown in Eq. 2 (Gavrilescu & Tudose, 1997):

$$\alpha_G = \frac{H_a - H_{na}}{H_a} \qquad (2)$$

where H_a and H_{na} are the aerated and non-aerated working liquid heights, respectively. U_L was determined by using a chronometer and measuring the displacement time of sodium polyacrylate spheres in the riser (Δx = 18 cm) and the downcomer (Δy = 12 cm). Bubble diameters were measured by *in situ* image capturing. The images were processed by using the WebPlotDigitizer software (Rohatgi, 2017).

2.1.3 Determination of the volumetric oxygen transfer coefficient

This k_La was estimated by employing the dynamic method (Bandyopadhyay *et al*., 1967), in which the dissolved oxygen concentration in the fluid was measured by using a YSI® Pro20 electrode. The sensor was located in the riser region of the airlift bioreactor and was calibrated under O_2 saturation conditions. First, the dissolved oxygen in the system was removed by bubbling N_2, then, air was supplied (at superficial velocities defined in section 2.1.2) into the bioreactor with simultaneous and continuous measurements of dissolved oxygen concentration registered by the electrode, until saturation condition was reached.

2.2 Numerical

2.2.1 Geometry and mesh

The model geometry (Fig. 2a) was built using the Ansys-DesignModeler® software, and the computational mesh was generated using the Ansys-Meshing® software. In order to extract average values in regions of interest within the reactor, five volumes were created in the computational mesh (Fig. 2b), namely, air, head, riser, downcomer and bottom. The boundary between the contact regions was conformal (i.e., the grid nodes coincide at the boundaries). The optimal number of elements in the mesh was defined through a mesh independence analysis, which is described in detail in Section 3.2.
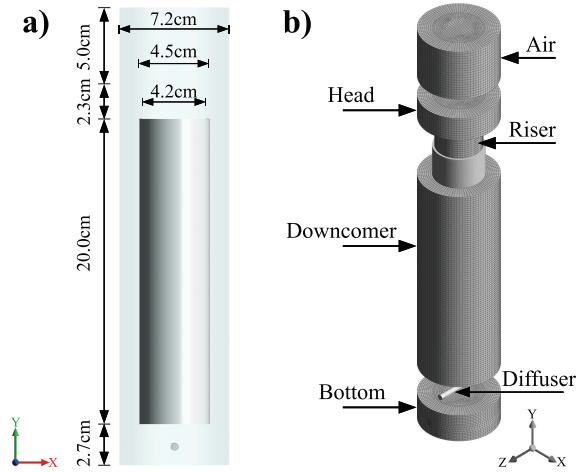
Fig. 2. Airlift bioreactor: a) geometry of the bioreactor, b) computational mesh.

2.2.2 Transport equations

The transient gas-liquid flow was modeled by using the Eulerian-Eulerian model, in which the mass transport Eq. (3) and momentum transport Eq. (4) are solved for each phase q, where $q = G$ (gas phase) and L (liquid phase) (Du *et al.*, 2006):

$$\frac{\partial \alpha_q \rho_q}{\partial t} + \nabla \cdot \left(\alpha_q \rho_q \vec{v}_q\right) = \sum_{p=1}^{n}\left(\dot{m}_{pq} - \dot{m}_{qp}\right), \tag{3}$$

$$\frac{\partial \alpha_q \rho_q \vec{v}_q}{\partial t} + \nabla \cdot \left(\alpha_q \rho_q \vec{v}_q \vec{v}_q\right) = \nabla \cdot \tau_q - \alpha_q \nabla P + \alpha_q \rho_q \vec{g}$$
$$+ \sum_{p=1}^{n}\left(\vec{R}_{pq} + \dot{m}_{pq}\vec{v}_{pq} - \dot{m}_{qp}\vec{v}_{qp}\right) + \vec{F}_q + \vec{F}_{L,q} + \vec{F}_{V,q}, \tag{4}$$

where for phase q, α_q is the volume fraction, ρ_q the density, $\vec{v}_q$ the velocity vector, $\dot{m}_{pq}$ is the mass transport from the pth to qth phase, and $\dot{m}_{qp}$ is the rate mass transport from phase q to phase p. In addition, P is the pressure, $\vec{g}$ is the gravity constant, $\vec{R}_{pq}$ is the interaction force between the two phases, $\vec{F}_q$ is an external body force (e.g., the Coriolis and the centrifugal force), $\vec{F}_{L,q}$ is a lift force, $\vec{F}_{V,q}$ is a virtual mass force, τ_q is the qth phase stress-strain tensor. This latter can be expressed as follows (Bowen, 1976):

$$\tau_q = \alpha_q \mu_{q,eff}\mathbf{D}, \tag{5}$$

where $\mu_{q,eff}$ is the effective viscosity of the phase q, which consists of a molecular viscosity (μ_q) and a turbulent viscosity ($\mu_{q,T}$), i.e.,

$$\mu_{q,eff} = \mu_q + \mu_{q,T}. \tag{6}$$

$\mathbf{D}$ is the deformation rate tensor, which can be written as:

$$\mathbf{D} = \left[\nabla \vec{v}_q + (\nabla \vec{v}_q)^T\right]. \tag{7}$$

The generalized molecular viscosity $[\mu_q(\dot{\gamma})]$ is a function of the magnitude of the deformation rate tensor ($\dot{\gamma}$), defined as

$$\dot{\gamma} = \sqrt{\frac{1}{2}\mathbf{D} : \mathbf{D}}. \tag{8}$$

On the other hand, the mathematical relations for the turbulent viscosity are presented in Section 2.2.4.

In this work, it is assumed that the only external volume force that contributes to the flow is the gravity, i.e., $\vec{F}_q = 0$. It is considered that the lift force is insignificant compared to the drag force, thus $\vec{F}_{L,q} = 0$, and the virtual mass force was considered constant, $\vec{F}_{V,q} = 0.5$. The interfacial force was computed by (Roco, 1993):

$$\sum_{p=1}^{n}\vec{R}_{pq} = \sum_{p=1}^{n}K_{pq}(\vec{v}_p - \vec{v}_q), \tag{9}$$

where K_{pq} is the interface momentum exchange coefficient, which, in turn, was calculated as follows (Roco, 1993):

$$K_{pq} = \frac{3}{4}\rho_q \alpha_q \alpha_p \frac{C_D}{d_b}\left|\vec{v}_p - \vec{v}_q\right|. \tag{10}$$

Here, C_D is the steady drag coefficient.

2.2.3 Drag model

The drag coefficient was computed by using the Grace model (Schiller, 1933; Grace & TH, 1976; Clift *et al.*, 1978), which can be expressed as

$$C_D = \max\left[\min(C_{D_{ellipse}}, C_{D_{cap}}), C_{D_{sphere}}\right]. \tag{11}$$

In Eq. (11), $C_{D_{ellipse}}$, $C_{D_{cap}}$ and $C_{D_{sphere}}$ are defined as follows:

$$C_{D_{sphere}} = \frac{4}{3}\frac{gd_b}{U_t^2}\frac{(\rho_q - \rho_p)}{\rho_q}, \tag{12}$$

$$C_{D_{cap}} = \frac{8}{3} \tag{13}$$

and

$$C_{D_{sphere}} = \begin{cases} \frac{24}{Re}, & Re < 0.01 \\ \frac{24}{Re}(1 + 0.15Re^{0.687}), & Re \geq 0.01 \end{cases} \tag{14}$$

where

$$U_t = \frac{\mu_q}{\rho_q d_b} Mo^{-0.149}(J - 0.857); \qquad (15)$$

Mo is the Morton number, given by

$$Mo = \frac{\mu_q^4 g}{\sigma^3} \frac{\rho_q - \rho_p}{\rho_q^2}; \qquad (16)$$

σ is the surface tension, and J is given by a piecewise function;

$$J = \begin{cases} 0.94 H^{0.757}, & 2 < H \le 59.3 \\ 3.42 H^{0.441}, & H > 59.3 \end{cases}, \qquad (17)$$

where

$$H = \frac{4}{3} Eo Mo^{-0.149} \left(\frac{\mu_q}{\mu_{ref}}\right)^{-0.14}, \qquad (18)$$

where Eo is the Eötvös number, given by

$$Eo = \frac{g(\rho_q - \rho_p)d_b^2}{\sigma}, \qquad (19)$$

and $\mu_{ref} = 0.0009$ Pa · s, Re is the bubble Reynolds number, and it is given by

$$Re = \frac{\rho_q |\vec{v}_p - \vec{v}_q| d_b}{\mu_q}, \qquad (20)$$

where d_b is the bubble diameter. Experimental bubble sizes used in simulations for the different flow rates evaluated in this work are show in Table 2. In Eq. (20), $|\vec{v}_p - \vec{v}_q|$ is the velocity between phases.

2.2.4 Turbulence model

The turbulence inside the reactor was simulated with the standard $\kappa - \epsilon$ model. In this model, the turbulence viscosity for the liquid phase can be computed by using (Šimčík *et al.*, 2011)

$$\mu_{T,L} = \rho_L C_\mu \frac{\kappa_L^2}{\varepsilon_L}. \qquad (21)$$

The turbulence kinetic energy (κ_L) and turbulence dissipation rate (ε_L) are given by

$$\frac{\partial \alpha_L \rho_L \kappa_L}{\partial t} + \nabla \cdot (\alpha_L \rho_L \vec{v}_L \kappa_L) = \nabla \cdot \left[\alpha_L \left(\mu_L + \frac{\mu_{T,L}}{\sigma_\kappa}\right)(\nabla \kappa_L)\right]$$
$$+ \alpha_L G_{L,\kappa} - \alpha_L \rho_L \varepsilon_L, \qquad (22)$$

$$\frac{\partial \alpha_L \rho_L \varepsilon_L}{\partial t} + \nabla \cdot (\alpha_L \rho_L \vec{v}_L \varepsilon_L) = \nabla \cdot \left[\alpha_L \left(\mu_L + \frac{\mu_{T,L}}{\sigma_\varepsilon}\right)(\nabla \varepsilon_L)\right]$$
$$+ \frac{\alpha_L \varepsilon_L}{\kappa_L} (C_{1\varepsilon} G_{L,\kappa} - C_{2\varepsilon} \rho_L \varepsilon_L), \qquad (23)$$

where $G_{L,\kappa}$ is defined as

$$G_{L,\kappa} = \mu_{T,L} \left[\nabla \vec{v}_L + (\nabla \vec{v}_L)^T\right] : \nabla \vec{v}_L. \qquad (24)$$

Standard turbulent model constants were used in simulations: $C_\mu = 0.09$, $\sigma_\kappa = 1.0$, $\sigma_\varepsilon = 1.3$, $C_{1\varepsilon} = 1.44$ and $C_{2\varepsilon} = 1.92$. The turbulence viscosity for the gas phase was computed as

$$\mu_{T,G} = \frac{\rho_G}{\rho_L} \frac{\mu_{T,L}}{\omega}, \qquad (25)$$

where $\omega = 1.0$.

2.2.5 Numerical estimation of $k_L a$

The mass transfer resistance (k_L), multiplied with the specific surface area of the gas phase (a), yields the volumetric oxygen transfer coefficient ($k_L a$). The k_L was calculated by using Higbie's penetration theory (Higbie, 1935) [eq. (26)], which considers one-dimensional time-dependent diffusion of the transferred component from the interface to the bulk concentration. This calculation approach for the k_L has been widely used in various studies (Huang *et al.*, 2010; Wang *et al.*, 2011; Chen *et al.*, 2016; Teli & Mathpati, 2021) showing adequate experimental predictions.

$$k_L = 2 \left(\frac{D_{O_2}}{\pi}\right)^{1/2} \left(\frac{\rho_L \varepsilon}{\mu_L}\right)^{1/4}. \qquad (26)$$

In Eq. (26), an oxygen diffusion coefficient in water (D_{O_2}) of 2×10^{-9} m^2·s^{-1} (Bach *et al.*, 2017) was used. By assuming spherical bubbles, the specific surface area of the air is given by

$$a = \frac{6\alpha_g}{d_b}. \qquad (27)$$

From Eqs. (26) and (27), the following equation can be obtained:

$$k_L a = 12 \left(\frac{D_{O_2}}{\pi}\right)^{1/2} \left(\frac{\rho_L \varepsilon}{\mu_L}\right)^{1/4} \left(\frac{\alpha_g}{d_b}\right). \qquad (28)$$

2.2.6 Numerical solution

The unsteady numerical solution was implemented in ANSYS Fluent® Version 17.1 using the finite volume method (FVM). Non-slip boundary conditions were applied to all solid surfaces. Atmospheric pressure condition was set at the free surface of the liquid column. Coupled pressure-velocity was calculated by using the phase-coupled simple scheme.

Spatial discretization was achieved employing the second order upwind scheme. Momentum and volume fractions were approximated by the QUICK scheme. Turbulence parameters and time discretization were obtained employing the first order upwind scheme. A time step of 10^{-3} s was considered, which produced a maximum Courant number of 0.1 and 0.05 in the riser and in the downcomer, respectively.

3 Results and discussion

3.1 Bubble diameter

Table 2 shows experimental average bubble diameters (d_b) in the riser region as a function of U_S and fluid rheology. Measured bubble size ranges from 4.56 mm ±0.51 mm (tap water, U_S =0.2 cm·s^{-1}) up to 13.10 mm ±0.28 mm (CMC 0.50%wt/v, U_S =0.61 cm·s^{-1}). It is important to point out that the experimental equipment used in this study has been previously addressed in publications from our group (Sánchez-Vázquez *et al.*, 2015, 2017 and 2018), involving several multiphasic mixtures, including organic liquid phases and/or suspended solid particles containing immobilized microorganisms. These mixtures allowed to conclude that the used experimental setup in this study avoid stagnant zones in the draft tube region.

It can be seen that by increasing U_S or the CMC concentration, bubble diameter increases as well. It is important to emphasize that bubble breakup was not observed within the range of experimental conditions evaluated in this work. However, bubble coalescence increases with CMC concentration or U_S. This behavior is characteristic of small diameter columns, where viscous forces predominate and the system exhibits a tendency to coalesce (Godbole *et*

al., 1982). These results are in agreement with those reported by Deng *et al.* (2010), who attribute this effect to the fact that increasing the liquid viscosity leads to a decrease in the turbulence intensity.

On the other hand, it was observed that increasing U_S or the CMC concentration causes the initial distance between contiguous bubbles after their formation in the diffuser to be smaller. So, the mechanisms that cause bubbles to approach each other in the bubble train due to well-known viscous wake attraction effects are stronger (Katz & Meneveau, 1996; Ramírez-Muñoz *et al.*, 2011), and the bubble collision and subsequent coalescence rate of bubbles, as well as the average bubble diameters, increase.

Table 2. Experimental average bubble diameters (expressed in mm).

U_S [cm·s^{-1}]	Water	CMC 0.25%wt/v	CMC 0.50%wt/v
0.2	4.56±0.51	5.87±0.30	6.12±0.62
0.31	6.35±0.47	7.35±0.38	8.48±0.42
0.41	8.10±0.52	8.80±0.77	10.80±0.56
0.51	9.45±0.51	10.04±0.54	11.95±0.51
0.61	10.8±0.62	11.27±0.63	13.10±0.28

3.2 Mesh independence analysis

To estimate the influence of the number of grid elements on the simulation results, a mesh independence analysis was performed. To this end, six structured hexagonal meshes were generated, where the number of elements was progressively increased in each of the regions defined in Fig. 1b (air, head, riser, downcomer and bottom), as shown in Table 3. It was ensured that, for each increment in the mesh resolution, the number of elements in each defined region increases around twice.

Table 3. Number of elements for each region defined for the mesh independence analysis.

Mesh	#1	#2	#3	#4	#5	#6
Regions	**Number of elements**					
Air	3144	8000	18060	33200	62424	130260
Head	1572	4000	10320	16600	36414	86840
Downcomer	4800	9600	40320	71440	175500	488000
Riser	4480	12000	41040	68400	135135	282800
Bottom	11308	21409	44169	61624	116122	267710
Whole domain	25304	55009	153909	251264	525595	1255610
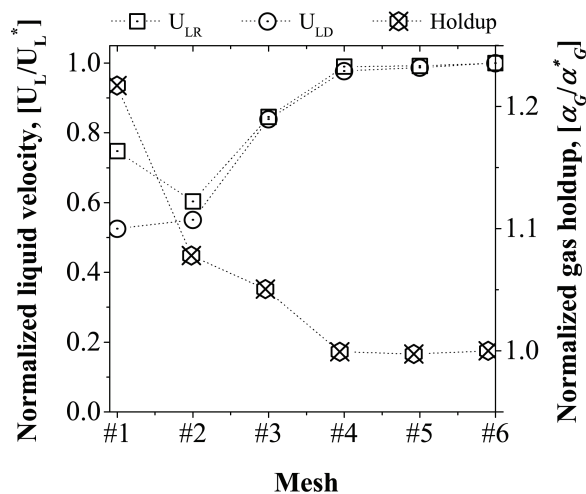
Fig. 3. Results of mesh independence analysis: U_S = 0.61 cm·s^{-1}, ρ = 997 kg·m^{-3} and μ = 10^{-3} Pa·s.

As evaluation criteria, average liquid velocities in the riser (U_{LR}) and downcomer (U_{LD}), as well as gas holdup values (α_G) were used. Fig. 2 shows these results for each defined mesh, which were normalized with respect to their corresponding densest mesh (mesh #6) values, i.e., U_{LR}^* = 13.5 cm·s^{-1}, U_{LD}^* = 7.49 cm·s^{-1} and α_G^* = 0.05. The maximum examined air superficial velocity (U_S = 0.61 cm·s^{-1}) and Newtonian fluid properties (ρ =997 kg·m^{-3} and μ = 10^{-4} Pa·s) were used for these determinations. Results suggest that U_{LR}, U_{LD} and α_G are independent of the mesh elements from Mesh #4 onwards. Therefore, this mesh ensures numerical accuracy while at the same time keeps computing time as low as possible. Therefore, the remaining simulations in this study were carried out by using this mesh of 251,264 elements.

3.3 Global hydrodynamics parameters

3.3.1 Liquid phase velocity

Fig. 4 shows numerical simulations of the effect of U_S and CMC concentration on global liquid phase velocities. To validate the numerical results, global experimental measurements of liquid phase velocities are also included in this Figure. The maximum relative difference between experimental and numerical values were 7.7% and 8.4%, in riser and downcomer, respectively, which are corresponding to CMC solution at 0.25%wt/v and U_S = 0.51 cm·s^{-1}. According to Fig. 4a, the liquid velocity in the riser (U_{LR}) increases with increasing U_S and decreases
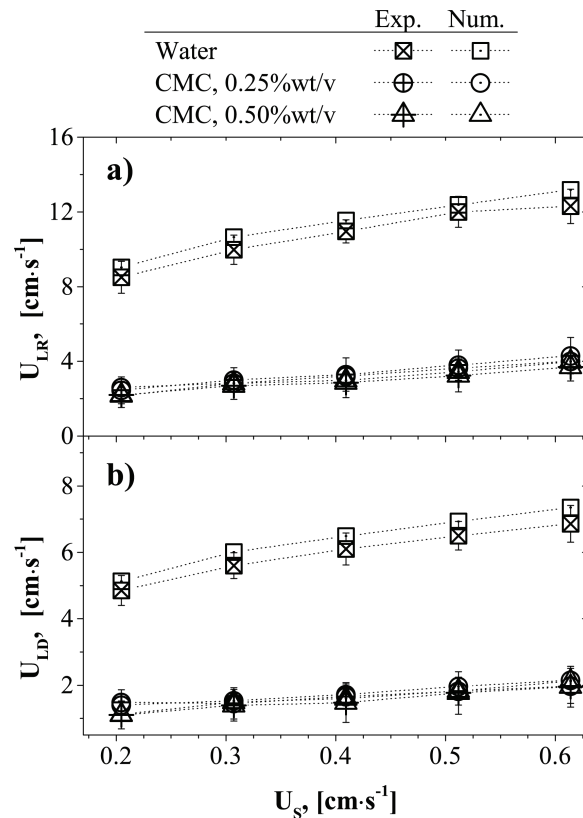

Fig. 4. Effect of U_S and CMC concentration on global liquid velocities: a) liquid velocity in riser (U_{LR}), and b) liquid velocity in downcomer (U_{LD}).

as CMC concentration increases. This is similar to what is observed in Fig. 4b for the liquid velocity in the downcomer (U_{LD}). Results from this work are in agreement with those reported by some authors, who analyzed the liquid circulation velocity in airlift bioreactors by experimentation (Verlaan *et al.*, 1986; Choi & Lee, 1993; Lu *et al.*, 1995) and numerical simulation (van Baten *et al.*, 2003; Wang *et al.*, 2006).

3.3.2 Liquid flow pattern

Fig. 5 shows the effect of the fluid rheology and U_S on the existing flow pattern in a particular plane inside the reactor, located at $0 \leq X \leq 3.6$ cm and $0 \leq$ and ≤ 14.7 cm. From this, a flow pattern characteristic of ALRs, similar to what is reported by some authors (Sokolichin *et al.*, 2004; Luo & Al-Dahhan, 2008; Luo & Al-Dahhan, 2008) can be seen, when water as a liquid medium is used, i.e., a fully developed up- and downflow in riser and downcomer, respectively.
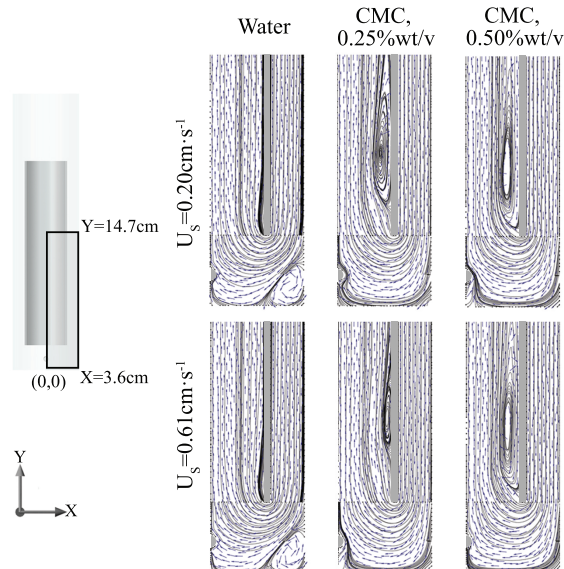
Fig. 5. Effect of CMC concentration and U_S on the numerical flow pattern.

However, at the bottom of the ALR, stagnation zones are formed, which turn out to be independent of the gas inlet velocities examined in this work. On the other hand, the formation of a recirculation loop region in the riser is evident when CMC aqueous solutions are used; this has not been reported previously, according to our literature review. This fact could be associated with the small inner diameter of the riser column used in the present study (i.e., 4.2 cm), which, together with the predominance of viscous forces, causes a significant drag effect in the riser wall surface, which induces the formation of recirculation loops.

The formation of recirculation loops causes a reduction in the riser and downcomer liquid velocity, which is more pronounced as the fluid viscosity increases, as shown in Fig. 5. By increasing U_S, the recirculation loops tend to decrease in size for the relatively low fluid viscosity (i.e., 0.25%wt/v CMC solution). The presence of stagnation zones and recirculation loops reduce the mixing efficiency in the reactor, and, according to our literature review, these phenomena have not been reported elsewhere. These results suggest that the effect of the ratio of the medium viscosity and U_S on the recirculation loop size warrant further investigation to improve airlift reactor mixing. However, this is beyond the scope of this work. Our results also highlight the practical application of our findings and open a new line of research addressed to improve the understanding and the performance of these systems.
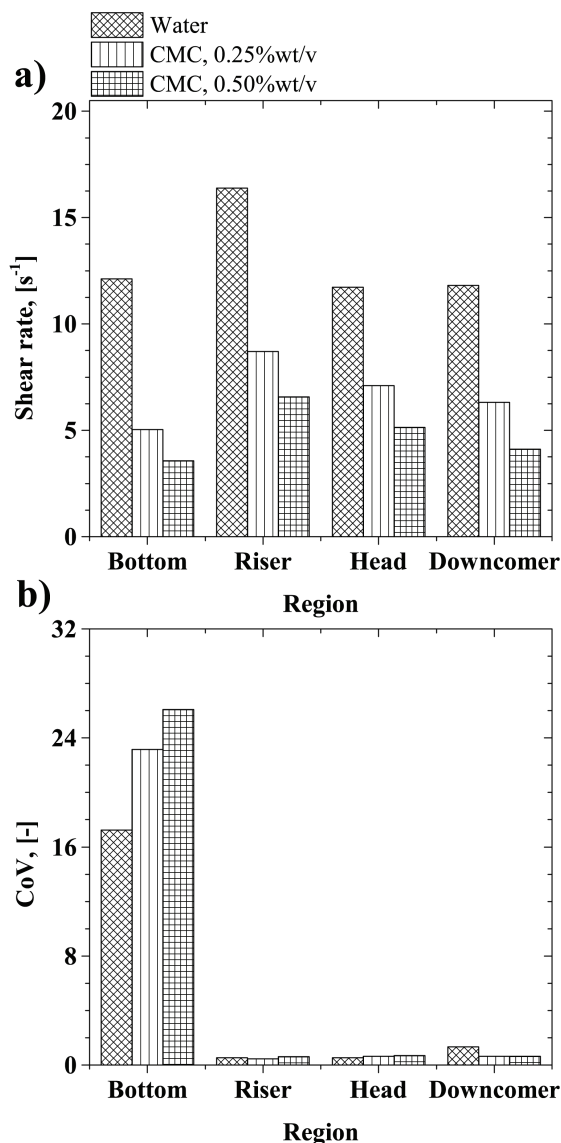

Fig. 6. Mean numerical values of shear rate and its respective coefficient of variation in different regions inside the airlift bioreactor at $U_S = 0.61$ cm·s^{-1}.

3.3.3 Average shear rate

Fig. 6a exhibits numerical average shear rate values at $U_S = 0.61$ cm·s^{-1} computed in the different regions previously defined in the computational mesh (i.e., bottom, riser, head and downcomer) for the three evaluated testing fluids. In addition, shear rate coefficient of variation (CoV) is included in Fig. 6b. CoV computed for each region represents the ratio of the shear rate standard deviation (σ) to the average shear rate value ($\overline{x}$) i.e., CoV= $\sigma/\overline{x}$, and it is included for comparing the degree of shear rate variation over

the different regions of the reactor.

According to Fig. 6a, highest average values of shear rate are in the riser region and decreases for each region as CMC concentration increases. On the other hand, it can be seen in Fig. 6b that the bottom region exhibits highest values of CoV, which are around one order of magnitude higher that those obtained in the remaining evaluated regions. This suggests that there exist higher shear rate values in the region close to the diffuser, which is in agreement with experimental measurements reported by Luo and Al-Dahhan (2008).

Recirculation loops located in the reactor´s bottom region with the Newtonian fluid (see the flow patterns shown in Fig. 5) could expose the microorganisms to high values of shear rate (or shear stress) by prolonged periods of time in this region thus causing damages in the microbial cell structure. These results highlight the practical application of our findings and suggests that a CFD approach can be used to establish safe operating conditions in airlift bioreactors in order to avoid adverse effects related to cell damages.

3.3.4 Global gas holdup

Fig. 7 shows experimental and numerical results of the effect of U_S and CMC concentration on the global gas holdup throughout the reactor, and in the different volumes previously defined in the computational mesh. Results for water are shown in Fig. 7a, and for CMC solutions at 0.25%wt/v and 0.50%wt/v are shown in Figs. 7b and 7c, respectively. The maximum relative difference between experimental and numerical values is 8.3%, which corresponds to 0.25%wt/v solution of CMC at $U_S = 0.61$ cm·s^{-1} (Fig. 7a). As expected, the highest values of gas holdup are obtained in the riser region, and their values increase with increasing CMC concentration or U_S. On the other hand, it has been reported, for similar experimental systems, that gas holdup decreases when CMC concentration increases (Gavrilescu & Tudose, 1997; Hwang & Cheng, 1997; Wei *et al*., 2000; Deng, Wang *et al*., 2010; Mendes & Badino, 2016; de Jesus *et al*., 2017). This effect has been attributed to the formation of large bubbles in highly viscous media with the absence of bubble breakup and presence of bubble coalescence, and consequently, the residence time becomes shorter and the gas holdup decreases. To gain fundamental insight on the origin of the discrepancy with the results from this work, a discussion is provided below.
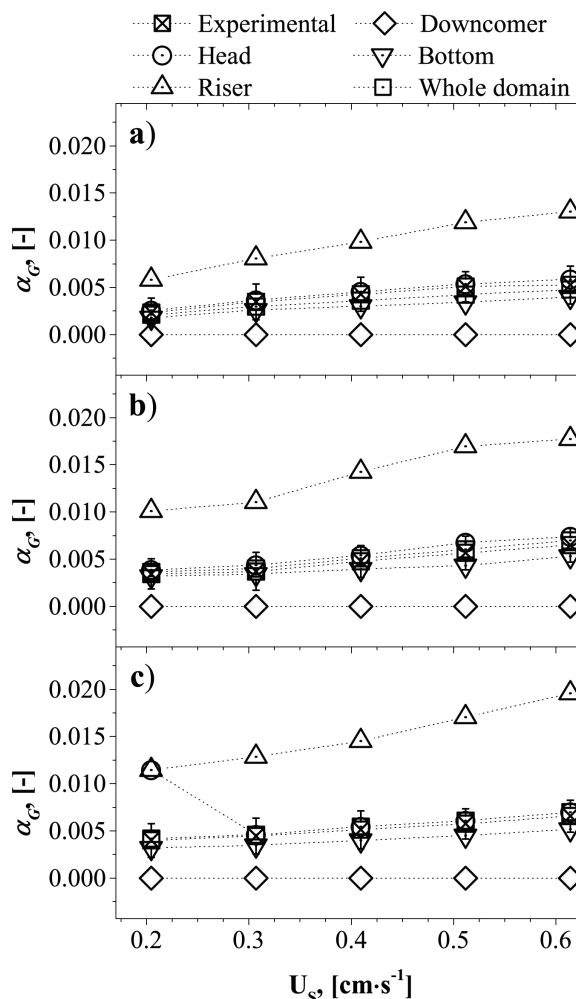

Fig. 7. Effect of U_S) and CMC concentrations on gas holdup (α_G): experimental and numerical data. a) Water, b) CMC 0.25%wt/v and c) CMC, 0.50%wt/v.

3.3.5 Gas phase velocity

Fig. 8 shows numerical results of the gas phase velocity in the riser region (U_{GR}) as a function of U_S and liquid viscosity. It can be seen that there exists a significant increase in the gas phase velocity as U_S increases. However, it is important to note that as the concentration of CMC (i.e., the medium viscosity) increases, the velocity of the gas phase decreases significantly. This effect can be attributed to two factors: (1) as the viscosity of the medium increases, the interfacial gas-liquid drag also increases, decreasing the velocity of the rising bubbles. (2) According to the numerical flow pattern shown in Fig. 5, air bubbles are retained for longer times in the recirculation loops formed in the riser region, and these recirculation loops are larger as the liquid
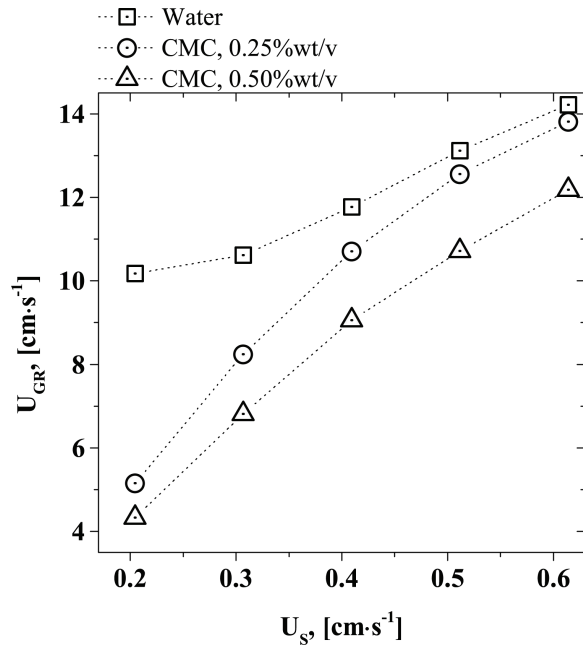
Fig. 8. Air velocity in the riser region from the numerical simulations.

Fig. 9. $k_L a$ versus gas outlet velocity (U_S) for different CMC concentrations.

viscosity increases. Therefore, both effects cause a decrease in the gas phase velocity in the riser region, i.e., an increase in the resident times of bubbles, and in the gas holdup.

3.3.6 Volumetric oxygen transfer coefficient

Fig. 9 shows numerical and experimental $k_L a$ values as a function of U_S and CMC concentrations. It can be seen that $k_L a$ increases when U_S also increases regardless of the fluid under consideration. However, the highest $k_L a$ value for each U_S evaluated is obtained with tap water, and it decreases with CMC concentration. This effect can be attributed to the fact that when the viscosity of the medium increases, the mass transfer resistance reduces [see eq. (26)]. In addition, an increase in bubble size (see Table 2) induces low values of the specific surface area [see Eq. (27)], and therefore, lower $k_L a$ values are obtained. These results are in agreement with experimental $k_L a$ values reported by Jiménez-González *et al.* (2015). Results from this work are in better approximation than those reported by Bach *et al.* (2017), who used an iterative method to calculate $k_L a$, which increases the number of simulations, and consequently, the computation time. The maximum relative difference between the experimental and numerical $k_L a$ value is 8.9%, which corresponds to the CMC solution at 0.25%wt/v.
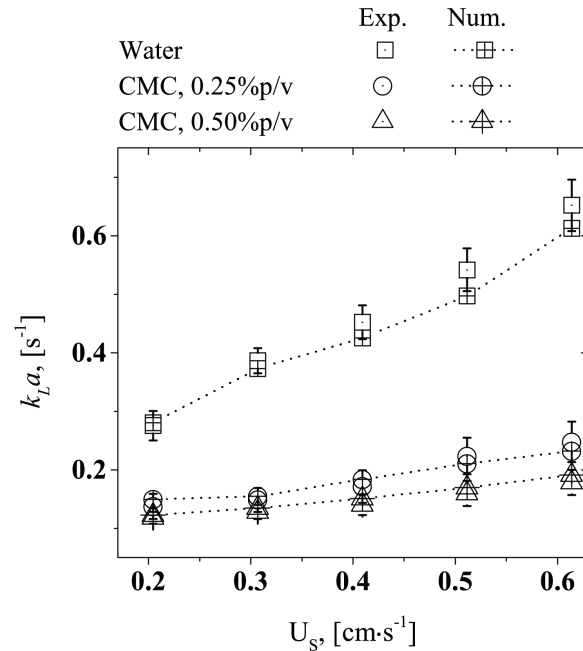
3.4 Local hydrodynamics parameters

3.4.1 Liquid phase velocity profiles

Fig. 10 shows the numerical radial profile of the liquid phase velocity in the riser and the downcomer as a function of CMC concentration at $U_S = 0.61$ cm·s^{-1}. The radius was normalized with respect to the internal column radius, i.e., $R_{it} = 3.6$ cm. The radial liquid phase velocity was extracted at three positions: the top (Y = 20.7 cm), the middle (Y = 12.7 cm), and the bottom (Y = 4.7 cm), as is depicted in Figs. 10a-c, respectively. Results show that the local liquid velocity decreases when CMC concentration is increased, both in riser and in downcomer. Furthermore, in the riser, the liquid velocity exhibits a parabolic decay in the axial analyzed region (4.7 cm ≤ and ≤ 20.7 cm) for the Newtonian and non-Newtonian fluids; however, for water, the velocity profiles at the three positions are higher. A slightly different tendency is evident for water in the bottom (Y = 4.7 cm), which can be attributed to this fluid having a low viscosity value. Therefore, at this position close to the diffuser, the viscous forces are not enough for damping chaotic movement induced by the diffuser.
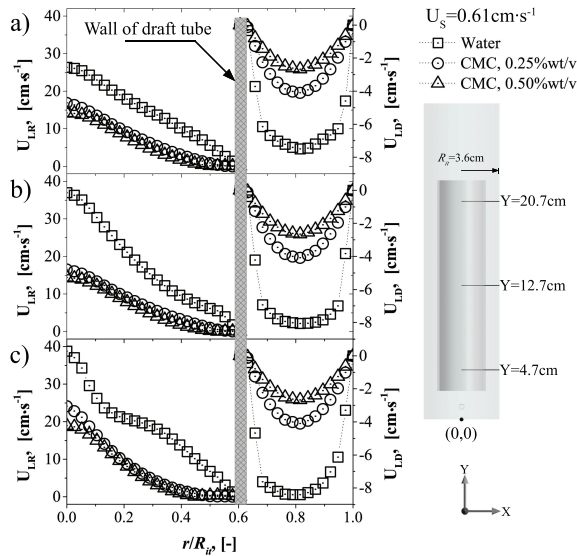
Fig. 10. Effect of CMC concentration on the numerical liquid velocity radial profile in different sections of the riser and downcomer. a) and = 20.7 cm, b) and = 12.7 cm and c) and = 4.7 cm.

On the other hand, in the downcomer, the liquid velocity for each examined fluid exhibits a fully developed parabolic profile in the analyzed region, which is characteristic of laminar flow. The profiles obtained in this work are in agreement with previous studies carried out in airlift bioreactors operating with water (Young *et al*., 1991; Jianping & Shonglin, 1998; Utiger *et al*., 1999; Jia *et al*., 2007). The region of the downcomer is critical in the oxygen mass transport, and it is well-known that there exists a poor radial mixing in the laminar regime. Therefore, the use of disturbing flow elements to induce chaotic motion of fluid particles in this region, e.g., helical flow promoters (Gluz & Merchuk, 1996; Schlötelburg *et al*., 1999; Särkelä *et al*., 2019), could be necessary.

3.4.2 Gas holdup profiles

In Fig. 11, numerical radial profiles of gas holdup in the riser as a function of CMC concentration at U_S = 283 cm·s^{-1} are presented. The radial distance was normalized with respect to the internal radius of the draft tube, i.e., Rid = 2.1 cm. Three cross-sections at different heights of the riser region are analyzed, namely, the top (Y = 20.7 cm), the middle (Y = 12.7 cm) and the bottom (Y = 4.7 cm), which are included in Fig. 10 a), b) and c), respectively.
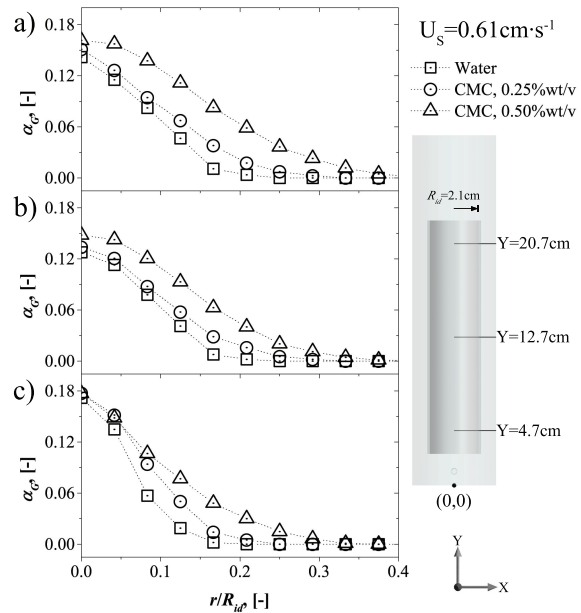

Fig. 11. Numerical results of the effect of CMC concentration on the radial profile of gas holdup in different sections of the riser. a) and = 20.7 cm, b) and = 12.7 cm and c) and = 4.7 cm.

The profiles obtained show that the gas holdup is higher in the riser center, and it decreases as the radius approaches the concentric tube wall. These results are qualitatively in agreement with previous studies (Fischer *et al*., 1994; Jianping & Shonglin, 1998; Schweitzer *et al*., 2001; Deng, Wang *et al*., 2010). However, as in the global gas holdup behavior, in the present study, the local gas holdup also increases with the CMC concentration. The existing higher gas holdup in top regions of the riser could be associated with experimental systems where the wake-induced attraction effect of preceding bubbles induces a high concentration of bubbles in the column top region, which has been reported previously for an air-water system [see Fig. 2 from Katz and Meneveau (1996)].

Conclusions

Experiments and unsteady three-dimensional simulations were carried out to describe in detail the hydrodynamics of an internal-loop airlift reactor by using Newtonian and non-Newtonian (shear-thinning) fluids. A good agreement between global experimental and numerical values of holdup and liquid velocity was obtained. The maximum relative difference for the

holdup and volumetric oxygen transfer coefficient was 8.3% and 8.9%, respectively, and for liquid velocity was 7.7% in the riser and 8.5% in the downcomer.

An increase in the CMC concentration induces the coalescence of bubbles in the riser region and the diameter of the bubble increases. According to the numerical results, the oxygen transfer resistance decreases as the CMC concentration increases. On the other hand, the increase in the bubble diameter induces low specific surface area, and therefore, the volumetric oxygen transfer coefficient decreases when the medium viscosity increases.

Results show that viscous forces predominate in the riser region with a coalescing tendency. This fact, together with the small inner diameter of the column employed in this work, induces a significant drag effect in the riser wall surface that favors the formation of recirculation loops for the two tested shear-thinning fluids. The recirculation loop size increases with the CMC concentration.

The presence of recirculation loops inside the riser was not observed with tap water. Recirculation loops in the bottom region together with the existing high shear rate values in this zone could induce cell damage by shear stress in bioprocesses carried out in airlift reactors. Recirculation loops in the riser region drastically reduce the overall liquid velocity in the reactor and the gas phase velocity in the riser. Therefore, bubble retention times and the holdup increase with CMC concentration. The downcomer region exhibits a nearly fully-developed laminar flow, which might be associated with a poor radial mixing in this region.

Results from this work show that CFD tools are key in gaining a fundamental understanding of local phenomena at a relatively low cost. These results are otherwise difficult to explain using experimental tools only.

Acknowledgments

Nomenclature

C_D	Drag coefficient [-]
d_b	Bubble diameter [cm]
Eo	Eötvös number [-]
$\vec{F}$	Body force [N·m^{-3}]
$\vec{F}_L$	Lift force [N·m^{-3}]
$\vec{F}_V$	Virtual mass force [N·m^{-3}]
H_a	Aerated working liquid height [cm]
H_{na}	Non-aerated working liquid height [cm]
k	Consistency index [Pa·s^n]
K	Interphase momentum exchange coefficient [kg·m^{-3}·s^{-1}]
k_La	volumetric oxygen transfer coefficient [s^{-1}]
$\dot{m}$	Rate mass transport [kg·m^{-3}·s^{-1}]
Mo	Morton number [-]
n	Flow index [-]
$\vec{R}$	Interaction force between phases [N·m^{-3}]
Re	Reynolds number [-]
R_{ic}	Internal column radius [cm]
U_L	Liquid-phase velocity [cm·s^{-1}]
U_{LR}	Liquid-phase velocity in riser [cm·s^{-1}]
U_{LD}	Liquid-phase velocity in downcomer [cm·s^{-1}]
U_S	Gas-phase intel velocity [cm·s^{-1}]
$\vec{v}$	Velocity vector [cm·s^{-1}]
X	Radial distance [m]
Y	Axial distance from the bottom [m]

Greek letters

α_G	Gas holdup [-]
ε	Turbulence dissipation rate [m^2·s'-3]
$\dot{\gamma}$	Shear-rate [s^{-1}]
κ	Turbulence kinetic energy [m^2·s^{-2}]
μ	Molecular viscosity [Pa·s]
μ_a	Apparent viscosity [Pa·s]
μ_{eff}	Effective viscosity [Pa·s]
μ_T	Turbulent viscosity [Pa·s]
ρ	Density [kg·m^{-3}]
σ	Surface tension coefficient [N·m^{-1}]
τ	Shear-stress [Pa]
$\boldsymbol{\tau}$	Stress-strain tensor [Pa]
Δx	Displacement in riser [cm]
Δy	Displacement in Downcomer [cm]

Abbreviations

ALR	Airlift Reactor
CFD	Computational Fluids Dynamics
CMC	Carboxy-Methyl-Cellulose
CoV	Coefficient of Variation
EL-ALR	External-loop Airlift Reactor
FVM	Finite Volume Method
IL-ALR	Internal-loop Airlift Reactor
QUICK	Quadratic Upstream Interpolation for Convective Kinematics
RNG	Re-Normalization Group

References

Bach, C., Yang, J., Larsson, H., Stocks, S.M., Gernaey, K.V., Albaek, M.O. and Krühne, U. (2017). Evaluation of mixing and mass transfer in a stirred pilot scale bioreactor utilizing cfd. *Chemical Engineering Science 171*, 19. https://doi.org/10.1016/j.ces.2017.05.001

Bandyopadhyay, B., Humphrey, A.E. and Taguchi, H. (1967). Dynamic measurement of the volumetric oxygen transfer coefficient in fermentation systems. *Biotechnology and Bioengineering 9*, 533. https://doi.org/10.1002/bit.260090408

Bowen, R. (1976). Theory of mixtures, aceringen. *Continuum Physics*, Academic Press, New York.

Cerri, M.O., Futiwaki, L., Jesus, C.D.F., Cruz, A.J.G. and Badino, A.C. (2008). Average shear rate for non-newtonian fluids in a concentric-tube airlift bioreactor. *Biochemical Engineering Journal 39*, 51. https://doi.org/10.1016/j.bej.2007.08.009

Clift, R., Grace, J.R., Weber, M.E. and Weber, M.F. (1978). *Bubbles, Drops, and Particles*. Academic Press,

Chen, Z., Jiang, Z., Zhang, X. and Zhang, J. (2016). Numerical and experimental study on the CO_2 gas-liquid mass transfer in flat-plate airlift photobioreactor with different baffles. *Biochemical Engineering Journal 106*, 129. https://doi.org/10.1016/j.bej.2015.11.011

Chisti, M.Y. (1989). Airlift bioreactors Elsevier Applied Science,

Choi, K.H. and Lee, W.K. (1993). Circulation liquid velocity, gas holdup and volumetric oxygen transfer coefficient in external-loop airlift reactors. *Journal of Chemical Technology and Biotechnology 56*, 51. https://doi.org/10.1002/jctb.280560110

de Jesus, S.S., Moreira Neto, J. and Maciel Filho, R. (2017). Hydrodynamics and mass transfer in bubble column, conventional airlift, stirred airlift and stirred tank bioreactors, using

viscous fluid: A comparative study. *Biochemical Engineering Journal 118*, 70. https://doi.org/10.1016/j.bej.2016.11.019

Deng, Z., Wang, T., Zhang, N. and Wang, Z. (2010). Gas holdup, bubble behavior and mass transfer in a 5m high internal-loop airlift reactor with non-Newtonian fluid. *Chemical Engineering Journal 160*, 729. https://doi.org/10.1016/j.cej.2010.03.078

Doran, P.M. (2013) Preface to the second edition. In: *Bioprocess Engineering Principles* (second edition), (P.M. Doran,ed.), Pp. vii. Academic Press, London.

Du, W., Bao, X., Xu, J. and Wei, W. (2006). Computational fluid dynamics (cfd) modeling of spouted bed: Assessment of drag coefficient correlations. *Chemical Engineering Science 61*, 1401. https://doi.org/10.1016/j.ces.2005.08.013

Esperança, M.N., Buffo, M.M., Mendes, C.E., Rodriguez, G.Y., Béttega, R., Badino, A.C. and Cerri, M.O. (2022). Linking maximal shear rate and energy dissipation/circulation function in airlift bioreactors. *Biochemical Engineering Journal 178*, 108308. https://doi.org/10.1016/j.bej.2021.108308

Fischer, J., Kumazawa, H. and Sada, E. (1994). On the local gas holdup and flow pattern in standard-type bubble columns. *Chemical Engineering Processes and Process Intensification 33*, 7. https://doi.org/10.1016/0255-2701(94)87002-0

Gavrilescu, M. and Tudose, R.Z. (1997). Hydrodynamics of non-newtonian liquids in external-loop airlift bioreactors. *Bioprocess Engineering 18*, 17. https://doi.org/10.1007/s004490050405

Gluz, M.D. and Merchuk, J.C. (1996). Modified airlift reactors: The helical flow promoters. *Chemical Engineering Science 51*, 2915. https://doi.org/10.1016/0009-2509(96)00174-1

Godbole, S.P., Honath, M.F. and Shah, Y.T. (1982). Holdup structure in highly viscous Newtonian and non-Newtonian liquids in bubble columns. *Chemical Engineering Communications 16*, 119. https://doi.org/10.1080/00986448208911090

Grace, J. and TH, N. (1976). Shapes and velocities of single drops and bubbles moving freely through immiscible liquids.

Han, M., Sha, Z., Laari, A. and Koiranen, T. (2017). Cfd-pbm coupled simulation of an airlift reactor with non-Newtonian fluid. *Oil Gas Science Technology - Reviews IFP Energies nouvelles 72*, 26.

Higbie, R. (1935). The rate of absorption of a pure gas into a still liquid during short periods of exposure. Trans. AIChE 31, 365.

Huang, Q., Yang, C., Yu, G. and Mao, Z.-S. (2010). Cfd simulation of hydrodynamics and mass transfer in an internal airlift loop reactor using a steady two-fluid model. *Chemical Engeneering Science 65*, 5527. https://doi.org/10.1016/j.ces.2010.07.021

Hwang, S.-J. and Cheng, Y.-L. (1997). Gas holdup and liquid velocity in three-phase internal-loop airlift reactors. *Chemical Engineering Science 52*, 3949. https://doi.org/10.1016/S0009-2509(97)88931-2

Jia, X., Wen, J., Feng, W. and Yuan, Q. (2007). Local hydrodynamics modeling of a gas-liquid-solid three-phase airlift loop reactor. *Industrial and Engineering Chemistry 46*, 5210. https://doi.org/10.1021/ie061697l

Jianping, W. and Shonglin, X. (1998). Local hydrodynamics in a gas-liquid-solid three-phase bubble column reactor. *Chemical Engineering Journal 70*, 81. https://doi.org/10.1016/S1385-8947(97)00120-4

Jiménez-González, A., Vargas-García, V., Lizardi-Jiménez, M.A. and Medina-Moreno, S.A. (2015). Evaluación de coeficientes volumétricos de transferencia de hidrocarburos poliaromáticos y oxígeno en sistemas multifásicos (líquido-líquido and líquido-líquido-gas): Efecto de la carga volumétrica de solventes biocompatibles. *Revista Mexicana de Ingeniería Química 14*, 723.

Kadic, E. and Heindel, T.J. (2014). Airlift bioreactors. *An Introduction to Bioreactor Hydrodynamics and Gas-Liquid Mass Transfer, 168*. https://doi.org/10.1002/9781118869703.ch8

Katz, J. and Meneveau, C. (1996). Wake-induced relative motion of bubbles rising in line. *International Journal of Multiphase Flow 22*, 239. https://doi.org/10.1016/0301-9322(95)00081-X

Lim, J.-S., Kim, J.-H., Kim, C. and Kim, S.-W. (2002). Morphological and rheological properties of culture broth of cephalosporium acremonium m25. *Korea-Australia Rheology Journal 14*, 11.

Lizardi-Jiménez, M.A. and Gutiérrez-Rojas, M. (2011). Assessment of the local hydrodynamic zones in a three-phase airlift reactor: Looking for the lowest liquid-phase Re. *Revista Mexicana de Ingeniería Química 10*, 59. https://doi.org/10.4090/juee.2008.v2n2.033040

Lizardi-Jiménez, M.A., Leal-Bautista, R.M., Ordaz, A. and Reyna-Velarde, R. (2015). Airlift bioreactors for hydrocarbon water pollution remediation in a tourism development pole. *Desalination Water Treatment 54*, 44. http://doi.org/10.1080/19443994.2013.876670

Lu, W.-J., Hwang, S.-J. and Chang, C.-M. (1995). Liquid velocity and gas holdup in three-phase internal loop airlift reactors with low-density particles. *Chemical Engineering Science 50*, 1301. https://doi.org/10.1016/0009-2509(95)98842-3

Luo, H.-P. and Al-Dahhan, M.H. (2008). Local characteristics of hydrodynamics in draft tube airlift bioreactor. *Chemical Engineering Science 63*, 3057. https://doi.org/10.1016/j.ces.2008.03.015

Luo, H.-P. and Al-Dahhan, M.H. (2008). Macro-mixing in a draft-tube airlift bioreactor. *Chemical Engineering Science 63*, 1572. https://doi.org/10.1016/j.ces.2007.11.027

Medina-Moreno, S.A., Conde-Báez, L., Jiménez-González, A., Aguilar-López, R., Rodríguez-Vázquez, R. and Tec-Caamal, E.N. (2020). Modelling hexadecane uptake strategies of a rhizospheric bacterial consortium under different hydrodynamic draft-tube airlift reactor conditions. *Biochemical Engineering Journal 160*, 107611. https://doi.org/10.1016/j.bej.2020.107611

Mendes, C.E. and Badino, A.C. (2016). Hydrodynamics of newtonian and non-newtonian liquids in internal-loop airlift reactors. *Biochemical Engineering Journal 109*, 137. https://doi.org/10.1016/j.bej.2016.01.007

Merchuk, J.C. and Garcia Camacho, F. (2010). Bioreactors: Airlift reactors. *Encyclopedia of Industrial Biotechnology 887*. http://doi.org/10.1002/9780470054581.eib144

Mohajerani, M., Mehrvar, M. and Ein-Mozaffari, F. (2012). Cfd analysis of two-phase turbulent flow in internal airlift reactors. *Canadian Journal of Chemical Engineering 90*, 1612. https://doi.org/10.1002/cjce.20674

Nalband, M. and Jalilnejad, E. (2019). 3d cfd simulation of gas hold-up and mass transfer in a modified airlift reactor with net draft tube. *International Journal of Chemical Reactor Engineering 17*. https://doi:10.1515/ijcre-2019-0060

Popović, M. and Robinson, C.W. (1988). External-circulation-loop airlift bioreactors: Study of the liquid circulating velocity in highly viscous non-Newtonian liquids. *Biotechnology and Bioengineering 32*, 301. https://doi.org/10.1002/bit.260320307

Ramírez-Muñoz, J., Salinas-Rodríguez, E., Soria, A. and Gama-Goicochea, A. (2011). Hydrodynamic interaction on large-reynolds-number aligned bubbles: Drag effects. *Nuclear Engineering Design 241*, 2371. https://doi.org/10.1016/j.nucengdes.2011.03.051

Roco, M.C. (1993). *Particulate Two-Phase Flow*. Butterworth-Heinemann, Boston.

Rohatgi, A. (2017). *Webplotdigitizer*. Austin, Texas, USA.

Sánchez-Vázquez, V., González, I. and Gutiérrez-Rojas, M. (2015). Electric field as pretreatment to enhance the activity of a whole-cell biocatalyst for hydrocarbon degradation in contaminated water. *Chemical Engineering Journal 260*, 37. https://doi.org/10.1016/j.cej.2014.08.036

Sánchez-Vázquez, V., Shirai, K., González, I. and Gutiérrez-Rojas, M. (2017). Fungal biocatalyst activated by an electric field: Improved mass transfer and non-specificity for hydrocarbon degradation in an airlift bioreactor. *Journal of Hazardous Materials 337*, 62. https://doi.org/10.1016/j.jhazmat.2017.05.001

Sánchez-Vázquez, V., Shirai, K., González, I. and Gutiérrez-Rojas, M. (2018). Polycyclic aromatic hydrocarbon-emulsifier protein produced by aspergillus brasiliensis (niger) in an airlift bioreactor following an electrochemical pretreatment. *Bioresources Technology 256*, 408. https://doi.org/10.1016/j.biortech.2018.02.043

Sandoval-Herazo, E., Saucedo-Rivalcoba, V., Gutiérrez-Rivera, B., Hernández-Martínez, R. and Lizardi-Jiménez, M. (2020). Diagnostic hydrocarbon pollution in veracruz beaches and airlift bioreactor as suggestion of remediation. *Revista Mexicana de Ingeniería Química 19*, 1227. https://doi.org/10.24275/rmiq/Bio851

Särkelä, R., Eerikäinen, T., Pitkänen, J.-P. and Bankar, S. (2019). Mixing efficiency studies in an airlift bioreactor with helical flow promoters for improved reactor performance. *Chemical Engineering Processes and Process Intensification 137*, 80. https://doi.org/10.1016/j.cep.2019.02.006

Schiller, L. (1933). A drag coefficient correlation. *Zeit. Ver. Deutsch. Ing. 77*, 318.

Schlötelburg, C., Popovic, M., Gluz, M. and Merchuk, J.C. (1999). Characterization of an airlift reactor with helical flow promoters. *Canadian Journal of Chemical Engineering 77*, 804. http://doi.org/10.1002/cjce.5450770504

Schweitzer, J.M., Bayle, J. and Gauthier, T. (2001). Local gas hold-up measurements in fluidized bed and slurry bubble column. *Chemical Engineering Science 56*, 1103. https://doi.org/10.1016/S0009-2509(00)00327-4

Šimčík, M., Mota, A., Ruzicka, M.C., Vicente, A. and Teixeira, J. (2011). Cfd simulation and experimental measurement of gas holdup and liquid interstitial velocity in internal loop airlift reactor. *Chemical Engineering Science 66*, 3268. https://doi.org/10.1016/j.ces.2011.01.059

Sokolichin, A., Eigenberger, G. and Lapin, A. (2004). Simulation of buoyancy driven bubbly flow: Established simplifications and open questions. *AlChE Journal 50*, 24. http://doi.org/10.1002/aic.10003

Teli, S.M. and Mathpati, C.S. (2021). Experimental and numerical study of gas-liquid flow in a sectionalized external-loop airlift reactor. *Chinese Journal of Chemical Engineering 32*, 39. https://doi.org/10.1016/j.cjche.2020.10.023

Utiger, M., Guy, C., Stuber, F., Duquenne, A.-M. and Delmas, H. (1999). Local measurements for the study of external loop airlift hydrodynamics. *Canadian Journal of Chemical Engineering 77*, 375. http://doi.org/10.1002/cjce.5450770225

Valdivia-Rivera, S., Lizardi-Jiménez, M.A., Medina-Moreno, S.A. and Sánchez-Vázquez, V. (2019). Multiphase partitioning airlift bioreactors: An alternative for hydrocarbon biodegradation in contaminated environments. *Advances and Applications of Partitioning Bioreactors*, 275.

van Baten, J.M., Ellenberger, J. and Krishna, R. (2003). Hydrodynamics of internal air-lift reactors: Experiments versus cfd simulations. *Chemical Engineering Processes and Process Intensification 42*, 733. https://doi.org/10.1016/S0255-2701(02)00076-4

Verlaan, P. (1987) Modelling and characterization of an airlift-loop bioreactor. Verlaan, S.l.

Verlaan, P., Tramper, J., Van't Reit, K. and Luyben, K.C.H.A.M. (1986). A hydrodynamic model for an airlift-loop bioreactor with external loop. *Chemical Engineering Journal 33*, B43. https://doi.org/10.1016/0300-9467(86)80052-1

Wang, T., Wang, J. and Jin, Y. (2006). A cfd-pbm coupled model for gas-liquid flows. *AlChE Journal 52*, 125. http://doi.org/10.1002/aic.10611

Wang, X., Jia, X. and Wen, J. (2011). Transient cfd modeling of toluene waste gas biodegradation in a gas-liquid-solid three-phase airlift loop reactor by immobilized pseudomonas putida. *Chemical Engineering Journal 172*, 735. https://doi.org/10.1016/j.cej.2011.06.052

Wei, C., Xie, B., Xiao, H. and Wang, D. (2000). Volumetric mass transfer coefficient of oxygen in an internal loop airlift reactor with a convergence-divergence draft tube. *Chemical Engineering Technology 23*, 597. http://doi.org/10.1002/1521-4125(200007)23:7<597::aid-ceat597>3.0.co;2-y

Wu, X. and Merchuk, J.C. (2003). Measurement of fluid flow in the downcomer of an internal loop airlift reactor using an optical trajectory-tracking system. *Chemical Engineering Science 58*, 1599. https://doi.org/10.1016/S0009-2509(02)00662-0

Xu, T., Jiang, X., Yang, N. and Zhu, J. (2015). Cfd simulation of internal-loop airlift reactor using emms drag model. *Particuology 19*, 124. https://doi.org/10.1016/j.partic.2014.04.016

Young, M.A., Carbonell, R.G. and Ollis, D.F. (1991). Airlift bioreactors: Analysis of local two-phase hydrodynamics. *AlChE Journal 37*, 403. https://doi.org/10.1002/aic.690370311